Supplementary Material for

Manganese substitution induced magnetic transformation and magnetoelectricity in SrFe$_{12}$O$_{19}$

M. R. Sahoo[a], A. Barik[a], R. Ghosh[a], S. Kuila[a], Sweta Tiwary[a], P. D. Babu[b], S. D. Kaushik[b] and P.N. Vishwakarma[a],*

[a] Department of Physics and Astronomy, National Institute of Technology, Rourkela, Odisha 769008, India
[b] UGC DAE Consortium for Scientific Research, Mumbai Centre, BARC, Mumbai 400085, India

X-ray diffraction

The room temperature XRD plots of $SrFe_{12-x}Mn_xO_{19}$ (x = 0, 3, 5, and 7) are shown in Fig. S1. All the peaks belong to strontium hexaferrite with space group $P6_3/mmc$. There is no sign of any impurity peak and detailed analysis is provided in the following paragraphs. However, the $SrFe_3Mn_9O_{19}$ (SrM9) prepared under similar conditions displayed the presence of secondary phases α-Fe_2O_3 (~6%) and $SrFe_2O_4$ (~8%), hence not considered for further studies. The parent compound SrM shows sharp crystalline peaks and with the increase of Mn content (x > 0) the peaks intensity gradually decreases, which might be due to decrease in the crystallinity or increase of strain, in the sample.
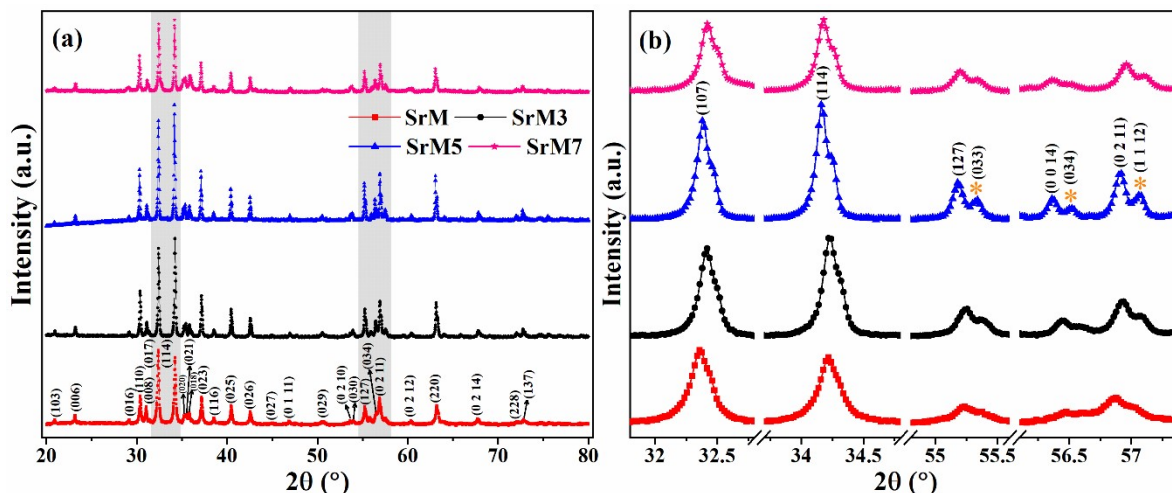
Fig. S1 (a) XRD profiles of SrM, SrM3, SrM5, and SrM7, and all the peaks are indexed with their miller indices. In Figure (b) magnified view of diffraction peaks in selected 2θ range are shown.

In the plot, prominent diffraction peaks at 2θ values of 30.37°, 32.35°, 34.20°, 37.16°, 40.43°, 42.55°, 55.22°, 56.85°, and 63.18° corresponding to the parent compound's diffraction planes (110), (017), (114), (023), (025), (026), (127), (0 2 11), and (220) respectively, are observed[1S-3S]. These characteristic reflections belong to the space group $P6_3/mmc$[1S]. The diffraction peaks of nearby d-values are not well resolved in the parent SrM, but with increasing Mn content, these peaks are now well resolved (highlighted). This might be due to the variation of lattice parameters 'a' and 'c'.

The XRD data are analyzed via the Rietveld refinement method, using Fullprof software. During the refinement, the background, instrumental parameter, scale factor, cell parameters, shape parameter, and position have been considered as variable parameters. The occupancy of each Fe/Mn site is also set as a free parameter. Lattice parameters obtained from the fitting are displayed in Table S1. The Rietveld refinement for all the samples is shown in Fig. S2 and the reliable factors obtained from the Rietveld refinement are also provided inside the plot. The low values of fitting parameters suggest that the studied sample is of better quality and refinements of XRD data are effective. The lattice parameters 'a' increases and 'c' decreases steadily by the 'Mn' substitution. The cell volume (V_{cell}) decreases with Mn content. The "c/a" value also slightly decreases from 3.92 with increasing "Mn" content in the compounds[28] (see Table S1).
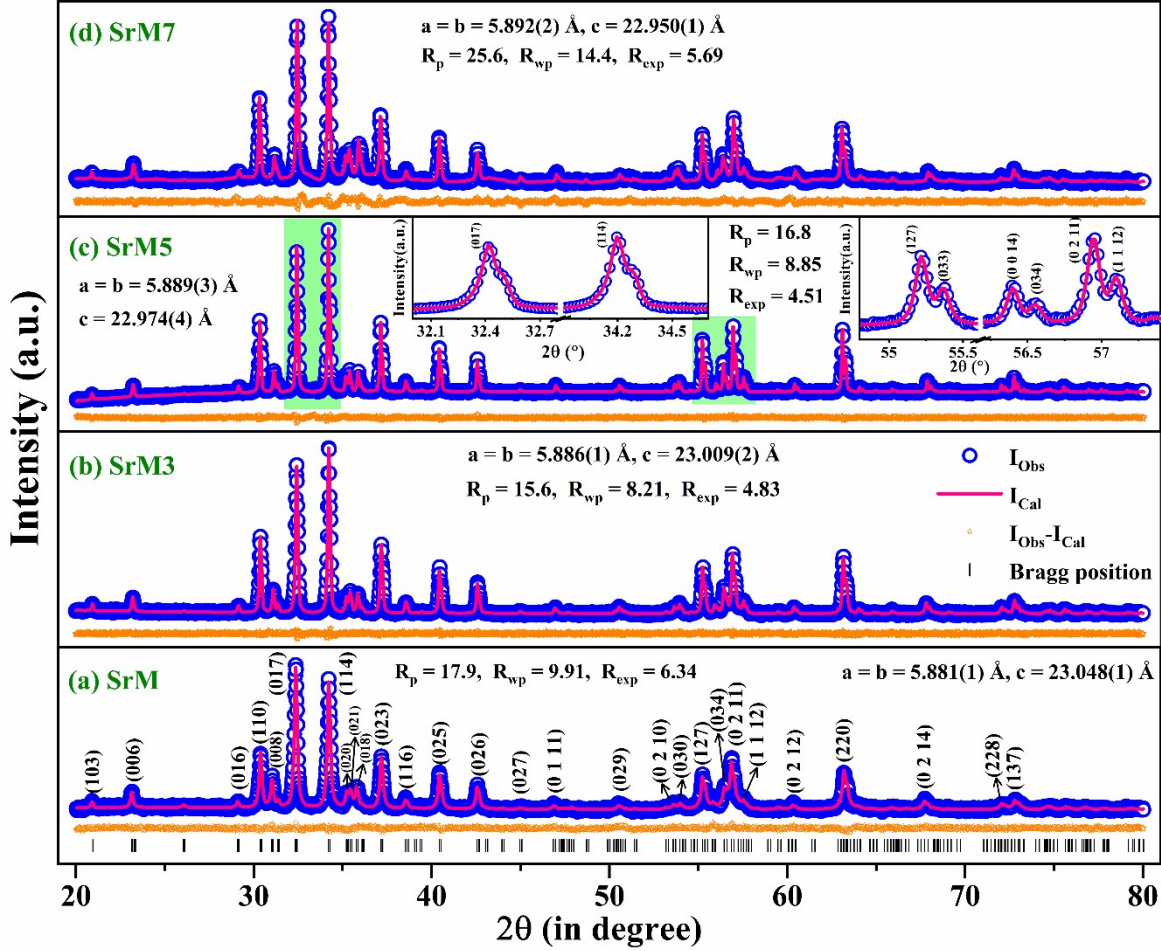
Fig. S2 Refined X-ray data of SrM, SrM3, SrM5, and SrM7 compounds, using the Rietveld method. All the XRD peaks are indexed with respective Miller indices. The highlighted area has been zoomed in and shown in the inset.

The lattice strain (ε) and average crystallite size (D) are calculated by following the Williamson- Hall method[3S],

$$\beta\cos\theta = \frac{K\lambda}{D} + 4\varepsilon\sin\theta$$

1S

Here, β is the full-width at half maxima of XRD peaks and θ is the position of the respective peaks. K = 0.9 is used assuming the grain size to be circular, λ (=1.544Å) is the wavelength of copper source X-ray and ε is the lattice strain. The slope (ε) and intercept $\left(\frac{K\lambda}{D}\right)$ obtained from the linear fitting to the graph plotted $4\sin\theta$ vs. $\beta\cos\theta$ gives the lattice strain and the crystallite size. The lattice strain (ε) obtained in this manner for SrM is 7.68×10⁻⁴. With an increase in Mn content in the sample, the ε-value gradually decreases for the SrM3 (3.02×10⁻⁴) and SrM5 (0.46×10⁻⁴) but for SrM7 the value (5.97×10⁻⁴) restores close to that of SrM. The crystallite size (D) so obtained for SrM is 88(2) nm and this value increased to 91(5) nm and 98(2) nm for SrM3, and SrM5 respectively. But it is interesting to note, for SrM7 the crystallite size jumps to approximately double of parent compounds size.

Table S1 Crystal structure parameters: lattice parameters, the crystallite size (D), and strain (ε) for all the compounds.

Sample	Lattice parameter (Å)		"c/a"	Cell volume	Crystallite size	Lattice strain
	'a' = 'b'	'c'		(V_{cell}) (Å^3)	(D) (nm)	(ε) ×10^{-4}
SrM	5.881(1)	23.048(1)	3.92(1)	690.39(4)	88(2)	7.68(1)
SrM3	5.886(1)	23.009(2)	3.91(1)	690.33(2)	91(5)	3.02(1)
SrM5	5.889(3)	22.974(4)	3.90(1)	689.94(2)	98(2)	0.46(1)
SrM7	5.892(2)	22.950(1)	3.90(5)	689.90(5)	162(1)	5.97(3)

The refinement of site occupation suggests that most of the substituted Mn go to the 12k-site. In precise, Mn preferably goes to the spin-up sites and very less to the spin-down sites i.e. $4f_1$ and $4f_2$, for all the Mn substituted compounds.

Neutron diffraction study

(a)

Fe1 = 2a octahedral, Fe2 = 2b bipyramid, Fe3 = $4f_1$ tetrahedral
Fe4 = $4f_2$ octahedral, Fe5 = 12k octahedral

(b)

Fe1 = 2a
Fe2 = 2b
Fe3 = $4f_1$
Fe4 = $4f_2$
Fe5 = 12k
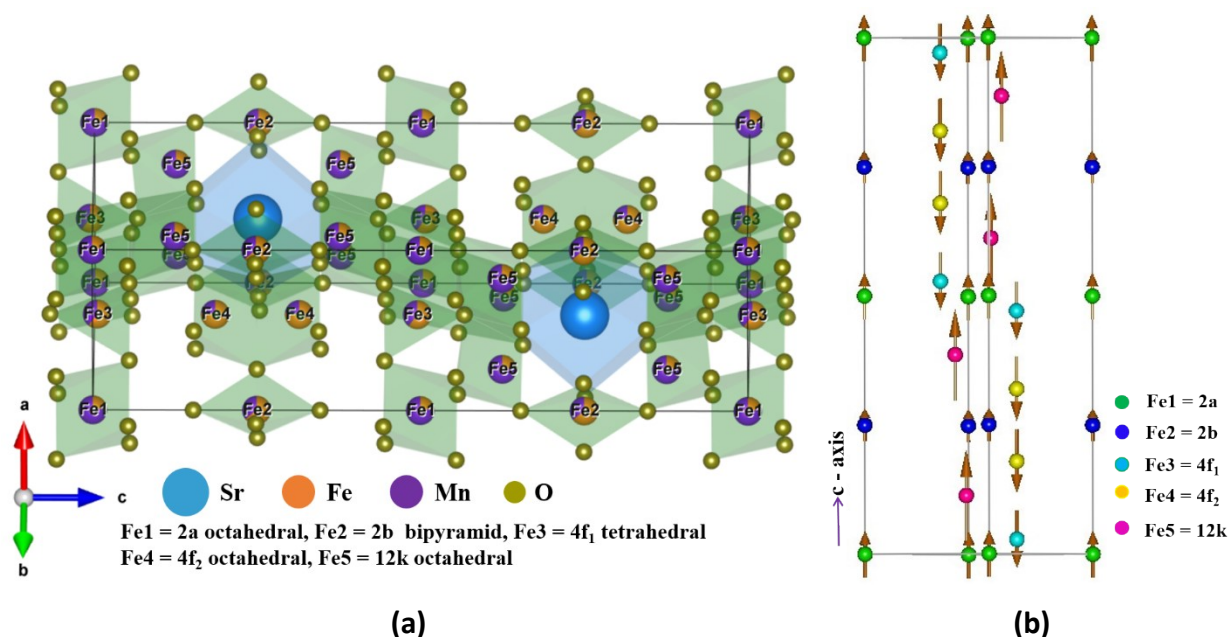
Fig. S3 (a) Schematic crystal structure of SrM7 obtained from ND refinement. Here blue, orange, dark purple and dark yellow circles are for strontium, iron, manganese, and oxygen ions respectively. The solid lines mark the boundary of the unit cell (or two formula units). The lattice orientation is shown by the arrow mark on the left side and different sites Wyckoff position is also written below. In figure (b) the magnetic spin arrangement of the SrM along the c-axis in a unit cell and the different colors circles are assigned to five sites[56].

The crystal structure has been plotted by the VESTA software, using the CIF file generated from the Rietveld refinement of SrM7 ND data. The crystal structure and magnetic spin arrangement of SrM7 is shown in Fig. S3. The different bond lengths and bond angles associated with different sites are extracted from these plots (i.e. SrM, SrM3, SrM5, and SrM5). These data are put together in the Table. S3. A sudden drop in some bond lengths at the 12k, 2b, and $4f_1$ sites is observed for the SrM7. This may have happened due to the increase in the concentration of Mn^{4+}. This can be seen in our upcoming X-ray photoelectron spectroscopy

(XPS) study, which confirms the rise in Mn^{4+} concentration with the increase in Mn substitution. In addition to this, the bond valence (V_{BV}) calculation at the 12k (Fe5), 2b (Fe2), and $4f_1$ (Fe3) sites for SrM7 show substantial change, indicating the rise in Mn^{4+} concentration at these sites.

Table S2 Occupancy percentage (relative to Fe) of Mn at Fe-sites, obtained from the refinement of ND data.

Lattice sites	'Mn' occupancy at different sites (in %)		
	SrM3	SrM5	SrM7
2a	40.8(2)	68.4(5)	79.5(2)
2b	18.2(5)	23.7(4)	34.9(4)
$4f_1$	27.9(1)	39.3(1)	40.2(1)
$4f_2$	11.5(1)	14.2(2)	23.7(4)
12k	32.2(5)	53.1(4)	76.5(2)

Table S3 Some of the most affected bond length and bond angles associated with various Fe-sites for the parent and the substituted compounds. These are obtained from ND.

Lattice Site	Bond length	SrM (Å)	SrM3 (Å)	SrM5 (Å)	SrM7 (Å)
2a	Fe1 - O4	1.98(4)	1.99(1)	2.01(2)	2.13(1)
2b	Fe2 - O1	2.32(3)	2.33(2)	2.24(3)	2.21(2)
	Fe2 - O3	1.85(4)	1.88(2)	1.82(3)	1.58(3)
$4f_1$	Fe3 - O2	1.86(4)	1.89(1)	1.92(4)	1.64(2)
	Fe3 - O4	1.91(2)	1.99(4)	1.98(3)	2.00(4)
$4f_2$	Fe4 - O3	2.04(5)	2.05(1)	2.07(1)	2.42(3)
	Fe4 - O5	1.98(1)	1.95(3)	1.95(1)	1.98(3)
12k	Fe5 - O1	1.97(3)	1.91(2)	1.97(1)	1.56(4)
	Fe5 - O2	2.15(1)	2.10(1)	2.02(1)	2.43(2)
	Fe5 - O4	2.10(1)	2.07(1)	2.09(1)	2.38(5)
	Fe5 - O5	1.96(4)	1.93(3)	1.92(4)	1.85(4)
Bond angle (°)	Fe1-O4-Fe3	125.2(4)	120.2(3)	119.8(4)	109.5(1)
	Fe1-O4-Fe5	96.4(1)	98.0(4)	96.9(4)	94.5(2)
	Fe2-O3-Fe4	139.3(2)	137.7(4)	137.5(2)	142.4(5)
	Fe3–O2–Fe5	125.8(2)	126.0(1)	123.8(5)	127.4(3)
	Fe4–O3–Fe4	81.4(3)	84.5(1)	84.9(3)	75.1(1)
	Fe5–O5–Fe5	98.2(1)	88.9(2)	98.2(4)	121.2(1)

The calculated bond valence (V_{BV}) and distortion (S) for all the compounds are provided in Table S4. For comparison, the same calculation by C.M. Fang[31] et al. has also been shown in the 1st row. They have used the room temperature XRD data from the K. Kimura[4S] et. al.

Table S4. The bond valence (V_{BV}) and the distortion (S) occurring at different sites are obtained from the ND data for all compounds.

Compound	RT data	Parameters	2a	2b	4f$_1$	4f$_2$	12k
SrM	Ref. [31]	V_{BV}	3.12(4)	2.82(1)	2.75(2)	3.07(1)	3.02(3)
	Ref. [4S]	S	13.75(3)	18.91(1)	7.86(4)	14.55(3)	15.69(2)
SrM	ND	V_{BV}	3.26(5)	2.81(3)	2.73(2)	3.02(4)	2.88(1)
		S	12.79(4)	20.46(2)	8.14(1)	14.60(3)	16.51(1)
SrM3	ND	V_{BV}	3.21(4)	2.58(4)	2.32(3)	3.14(3)	3.19(4)
		S	13.12(5)	21.18(4)	11.82(1)	14.04(1)	14.53(2)
SrM5	ND	V_{BV}	3.14(1)	3.07(1)	2.30(2)	3.09(1)	3.15(2)
		S	13.61(3)	17.43(4)	11.73(2)	14.63(3)	14.49(1)
SrM7	ND	V_{BV}	2.20(2)	5.48(1)	2.89(3)	2.13(4)	3.78(2)
		S	21.08(1)	18.02(3)	12.46(4)	28.19(2)	26.11(2)

Valence state conformation through X-ray photoelectron spectroscopy (XPS)
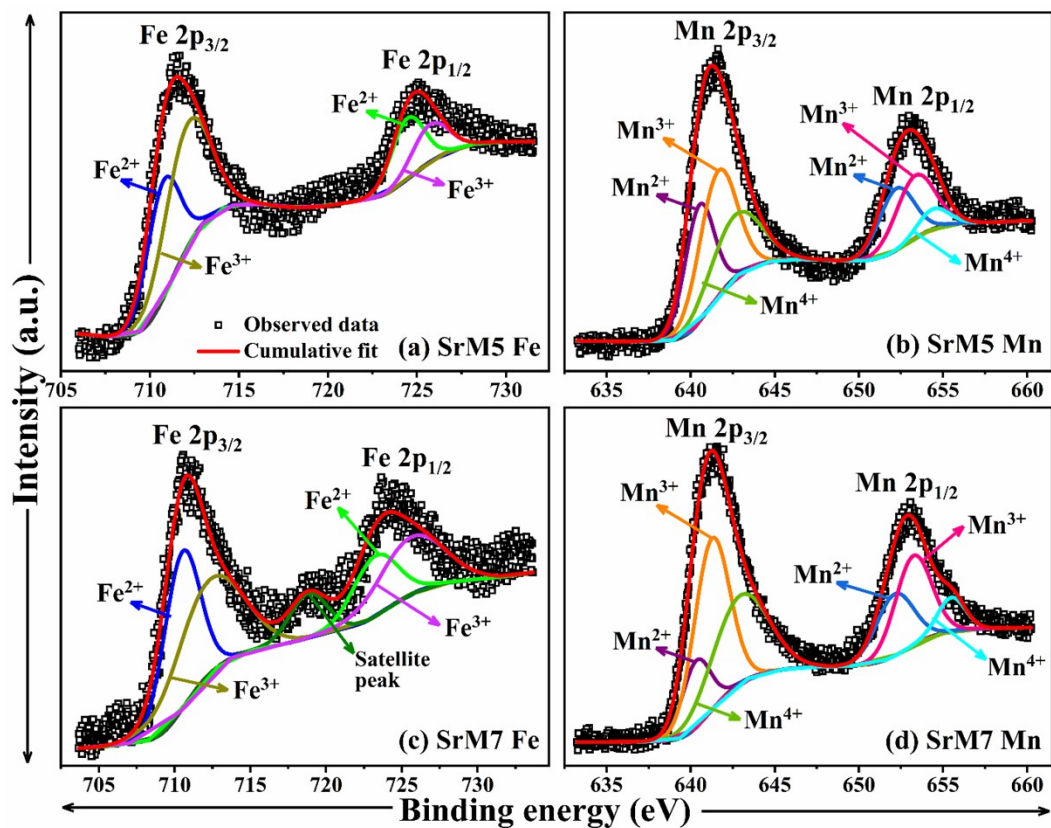
Fig. S4 High-resolution XPS spectrum of Fe, Mn in SrM5 and SrM7 compounds at room temperature.

The XPS characterization not only confirms the presence of elemental composition (i.e. Sr, Fe, Mn, and O) of SrM5, SrM7 but also gives information about the valence state of all the constituent elements. Here, in Fig. S4, the high-resolution XPS spectra of Fe,

and Mn are presented. The binding energy of carbon (C) '1s' peak i.e. 284.6 eV is used for the calibration of the total spectrum and then high-resolution peaks are fitted/deconvoluted using Origin software (peak fit pro) with Shirley function as background. The high-resolution spectra of Fe 2p and Mn 2p give two major peaks (due to spin-orbit coupling), named as Fe/Mn $2p_{3/2}$; $2p_{1/2}$. Each major peak of Fe and Mn are deconvoluted into two and three peaks respectively. The deconvoluted $2p_{3/2}$ peak for SrM5 are at 710.7 eV; 712.1 eV and that for SrM7 are at 710.4 eV; 712.3 eV. This indicates the presence of both Fe^{2+} and Fe^{3+}. Additional satellite peak is witnessed in Fe spectra of SrM7 at 718.8 eV. Similarly, the deconvoluted $2p_{3/2}$ peak of Mn for SrM5 and SrM7 are at 640.5 eV; 641.6 eV; 642.7 eV and 640.3 eV; 641.2 eV; 642.9 eV, confirming the existence of Mn at the +2, +3, and +4 states respectively. The same output is obtained from the 2nd major peak of Fe, and Mn having Fe in +2/+3 and Mn in +2/+3/+4 valence states. The percentage of Mn ions in different oxidation is calculated by the ratio of the area of one respective peak to the total area of peaks. The existence of Mn^{2+}, Mn^{3+}, and Mn^{4+} in SrM5 is ~30%, ~42%, and ~28%. In the case of SrM7, the Mn^{2+} ions percentage decreases to ~15% but the Mn^{3+}, and Mn^{4+} percentage increase to ~47% and ~38% respectively. Similarly, the existence of Fe^{2+} in SrM7 increases to ~47% from ~41% in SrM5, and Fe^{3+} presence drops with an increase in Mn percentage.

Surface Morphology

The average grain size from the FESEM images is obtained by the ImageJ software. The output result from ImageJ software plotted in histogram form is fitted with the Gaussian function.
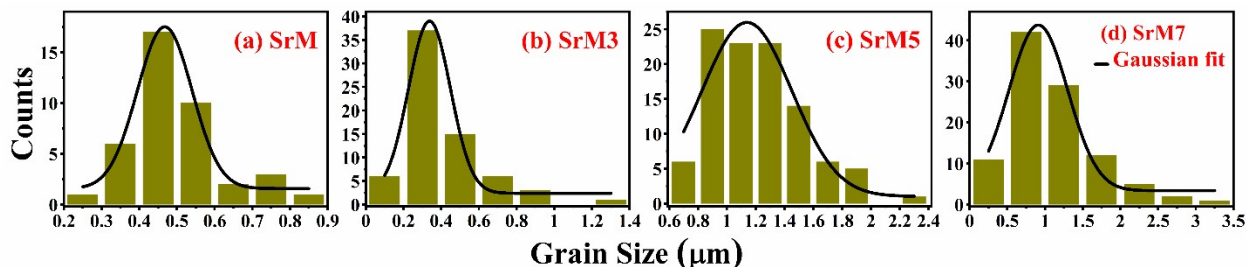
Fig. S5 The histogram image of (a) SrM, (b) SrM3, (c) SrM5, and (d) SrM7 grain size distribution obtained from the FESEM image with a Gaussian fit.

The relative density of all the samples are calculated with the formula,

$$Relative\ density = \left(\frac{Experimental\ density}{Theoretical\ density}\right) \times 100 \qquad 2S$$

where, the experimental densities of the samples are calculated from the respective pellet's mass divided by its volume. The pellets mass (with precision) is weighed using an electronic balance, and the volume of the pellet is measured using the formula $\pi r^2 h$, where 'r' is the radius of the pellet and 'h' is the thickness/height of the pellet. The theoretical density is extracted from the Rietveld refinement output file. Thereafter, the relative density of the compounds are calculated with Eq. 2S, and the result is presented in Fig. S6.
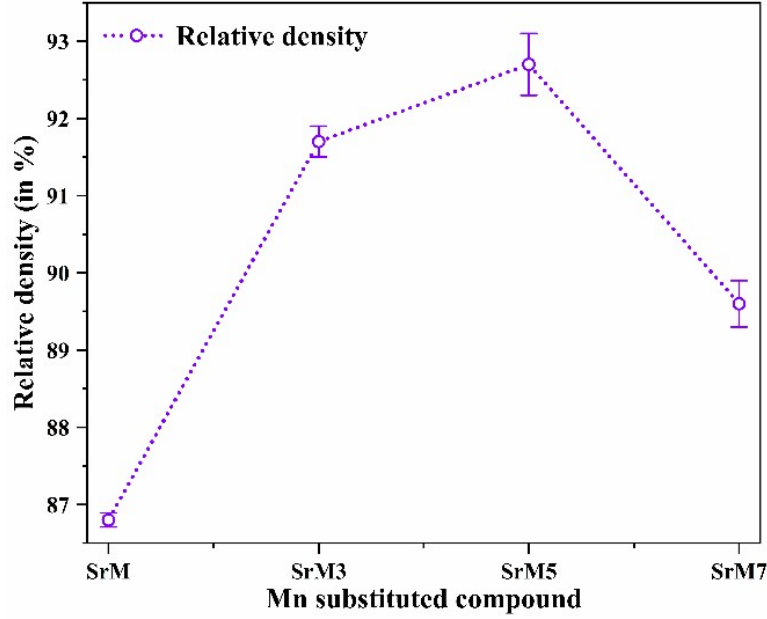
Fig. S6 Variation of relative density with the Mn substitution.

Magnetic study

For a magnetic system having non-zero magnetic anisotropy, the magnetization of the system (a special case of the Brillouin function with $J = 1/2$) is described by the reduced equation[42, 5S],

$$M = M_{sat}tanh(a) \qquad\qquad 3S$$

As a result, the M-H curve of SrM, SrM3, SrM5, and SrM7 in the magnetic field range -90 kOe to +90 kOe is fitted with,

$$M = M_{sat}\tanh\left(\frac{\mu}{K_BT}(H \pm H_c)\right)_{+ \chi H} \qquad\qquad 4S$$

Here 'χH' is added for the linear behavior at higher fields (i.e. paramagnetic contribution) and '$\pm H_c$' included for the magnetic coercivity. Fitting is done in such a manner that the saturation magnetization is reproduced, although the fitting does not exactly follow the observed data. The reason for the deviation of observed data with that of fitting is the strong magnetic anisotropy in present in all the compounds. For magnetic systems having non-zero anisotropy, the observed magnetization due to the rotation of spins in the field direction is given by,

$$M = M_{sat}\cos C \qquad\qquad 5S$$
$$\Rightarrow \cos C = M/M_{sat} = \eta \ (say)$$

where 'C' is the angle between magnetization (assumed to be in the direction of field) and the easy axis.

Earlier we saw that the saturation magnetization value obtained via eq. (2) was found undervalued and hence considered as M of eq. (4S). M_{sat} is taken as the value of observed magnetization at the highest field i.e., 90 kOe. This gives η = ~0.58, ~0.59, ~0.71,and ~0.72 resulting the angle 'C' ~54°, ~53°, ~45°, and ~44° for SrM, SrM3, SrM5, and SrM7 respectively. Thus, the undervalues saturation magnetization obtained via fitting of data using eq. (2), is multiplied by the factor 1/ η, to obtain the correct saturation magnetization and is denoted by M_s^{η}. Accordingly, the saturation magnetization for FiM1 (named as M_{s1}^{η}), and FiM2 (named as M_{s2}^{η})- phase is calculated and displayed in Fig. 9.

Again, the saturation magnetization obtained from the fitting (with the help of Eq.2) for FiM1 (named as M_{s1}), and FiM2 (named as M_{s2})- phase is displayed in along with the saturation magnetization obtained from the law of approach (LAS) i.e. M_s^{LAS} in the table S5. The saturation magnetization value at 3 K for SrM remains lower than 20 $\mu_B/f.u.$ and this may be due to the (i) measurements are done in absolute condition or (ii) existence of Fe in multivalence states (i.e. Fe^{2+}/Fe^{3+}).
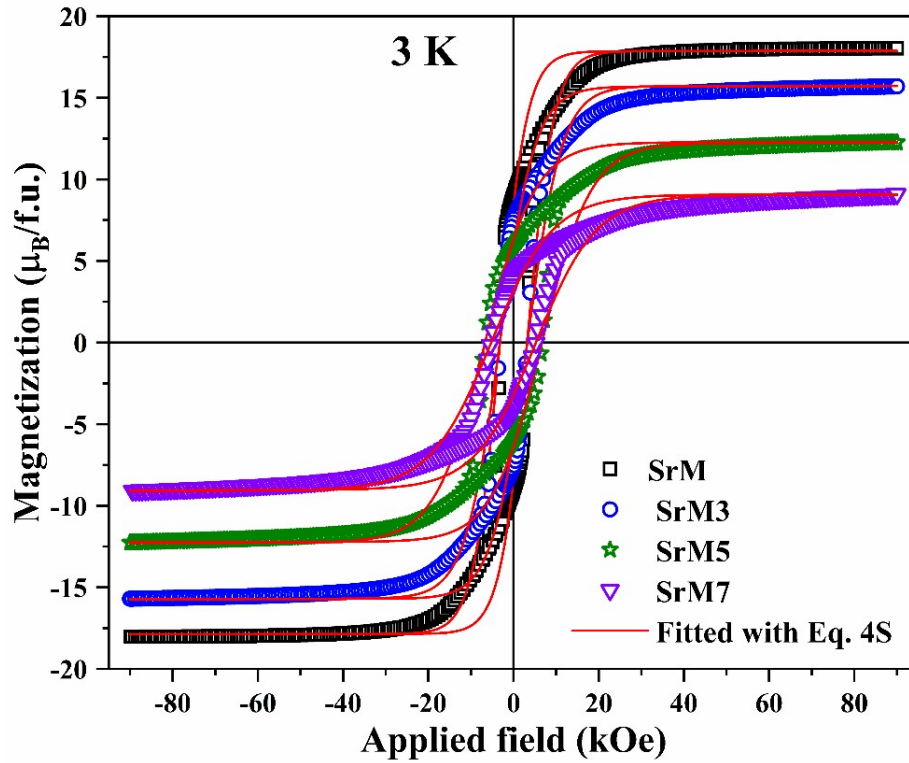
Fig. S7 Fitted M-H loop of SrM at room temperature by Eq. 4S.

Table S5. Comparative table for the saturation magnetization from the LAS method and form fitting for all the compounds at different temperatures. M_s: Saturation magnetization from 90kOe M-H plot. All saturation magnetization values are in $\mu_B/f.u.$ unit

Sample	T (K)	3	150	300	373	423	473	523	573	623	673	723
SrM	M_s	18.04	16.54									
	M_s^{LAS}	18.09(1)	16.58(4)	13.04(5)	10.92(4)	9.83(1)	8.76(2)	7.69(2)	6.69(5)	5.73(2)	4.40(1)	2.38(1)
	M_{s1}	10.37(1)	9.30(1)	7.46(2)	6.31(2)	5.60(3)	4.90(5)	4.27(3)	3.65(1)	3.05(2)	2.39(3)	1.46(2)
SrM3	M_s	15.72	13.15									
	M_s^{LAS}	15.93(1)	13.36(1)	7.85(2)	7.22(4)	6.27(3)	5.01(2)	4.07(3)	3.14(2)			
	M_{s1}	9.23(1)	7.49(3)	4.46(1)	3.99(3)	3.40(2)	2.70(2)	2.15(2)	1.66(4)			
SrM5	M_s	12.27	9.60									
	M_s^{LAS}	12.54(2)	9.89(4)	5.45(1)	4.32(3)	3.35(3)	2.35(2)	T=453K	2.55(3)			
	M_{s1}	8.27(4)	6.36(2)	3.61(1)	2.69(2)	1.85(1)	1.28(1)		1.40(2)			
	M_{s2}	3.42(5)	2.42(4)	1.61(1)	1.54(2)	1.27(2)						
SrM7	M_s	9.09	6.68									
	M_s^{LAS}	9.50(1)	7.05(2)	2.85(4)	1.69(3)	T=348K	2.03(1)	T=398K	1.39(4)	T=413K	1.04(5)	
	M_{s1}	6.52(4)	4.44(2)	1.21(1)	0.66(1)		0.75(4)		0.51(2)			
	M_{s2}	3.54(1)	3.37(4)	2.01(2)	1.43(2)		1.62(5)		0.88(5)		0.59(4)	

All the fitted parameters obtained from Eq. (3) are compiled in Table S6. As we have replaced the M_{s1}^{η} expression in Eq. (4). So for the purpose of comparison between the value of exponent 'P' of the Eq. (3) and Eq. (4) are listed in Table S6.

Table S6. The output parameters obtained from fitting the temperature varied M_{s1}^{η}, and H_{c1} with equation (3), and (4) respectively.

Output data		Equation (3)			Equation (4)
parameters ➡		$M_{s1}^{\eta}(0)$	$A \times 10^{-5}$	P	P
samples ⬇		μ_B / f.u.			
SrM		16.06(2)	5.31(2)	1.47(1)	1.56(3)
SrM3		10.39(3)	2.46(5)	1.62(4)	1.57(3)
SrM5		8.29(4)	4.38(5)	1.59(2)	1.56(1)
SrM7		3.35(4)	7.07(2)	1.56(1)	1.67(4)

The drop of saturation magnetization may also be understood in terms of the exchange constant J_{ex} $(= 3k_B T_\theta/2S(S+1))$ due to weak $Fe^{3+}- O^{2-} -Mn^{3+}$ interaction than the $Fe^{3+}- O^{2-} -Fe^{3+}$ interaction. To understand this in pictorial form, the Fe5 (12k-site) of strontium hexaferrite, is placed in between the other ions as shown in Fig. S8. The interaction of Fe5 with its neighbouring ions likes Fe1, Fe2, Fe3, and Fe4 are named as $J_{15}, J_{25}, J_{35},$ and J_{45} respectively. With the increase in Mn-substitution, the 12k site is more occupied by the Mn, which possesses a lower spin moment than the iron ion. As a result, the exchange interaction between the ions decreases. This causes drop in saturation magnetization with Mn substitution.
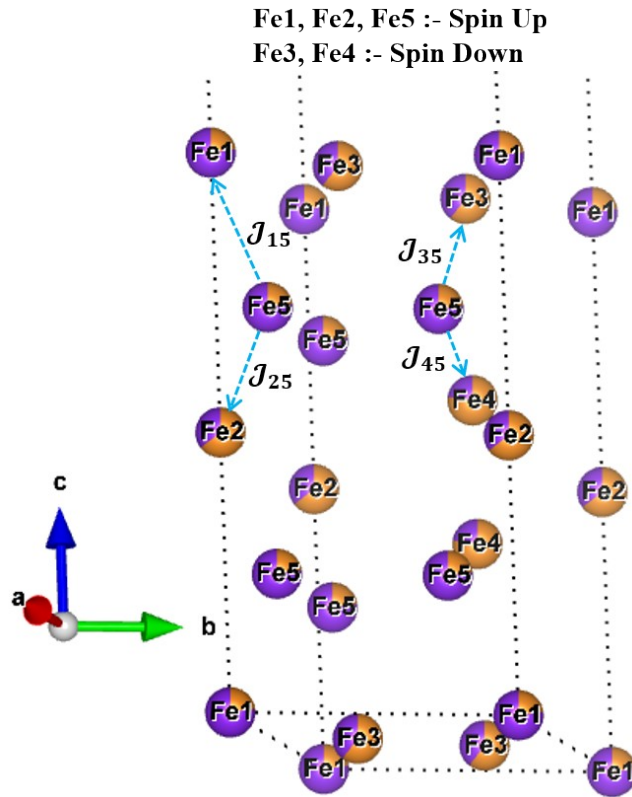
Fig. S8 Schematic diagram of SrM7 projected on a 2D-plane with the help of VESTA software (having boundary condition x = (0, 1), y = (0, 1), z = (0, 0.5)). Here we have shown the exchange interaction between the two iron ions (neighbor ions). Here orange and dark purple are for iron and manganese contribution respectively.

The M-H loop for SrM9 (shown in Fig. S9) displays a very thin loop, in contrary to SrM. This shows that SrM9 has completely transformed to FiM2- phase (i.e. R = 0). The M-H loop fitted through both the equations (i.e. Eq. (2) and Eq. (4S)) and both shows a good fit to the observed data. The saturation magnetization and coercivity value obtained from both the fitting are almost the same. The good fit to the M-H data of SrM9 with Eq. (4S) indicates the anisotropy effect has almost diminished in it.
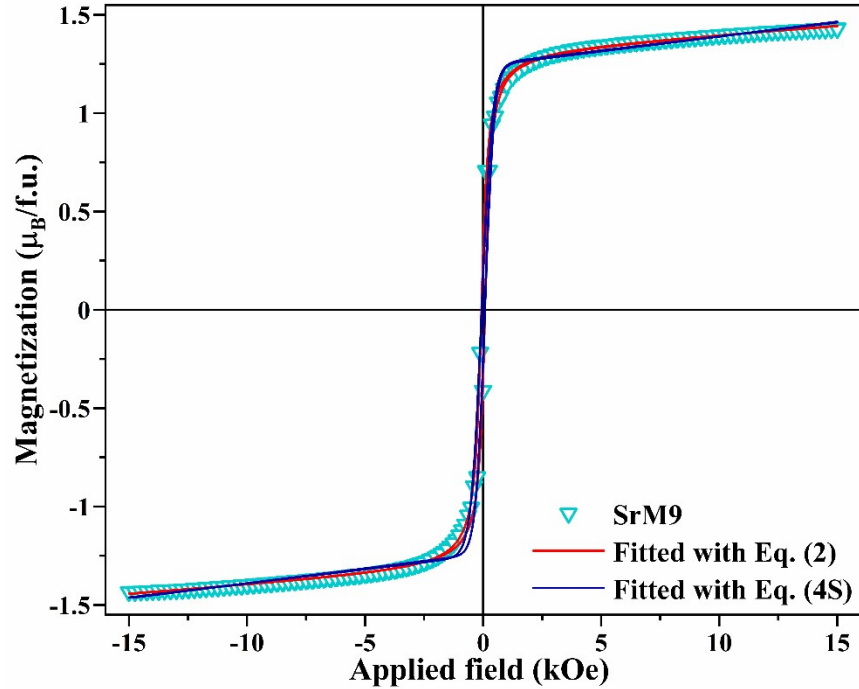
Fig. S9 M-H loop of SrM9 at room temperature. The red and blue line is for the fitted line.

Resistivity Study

The DC- resistivity (ρ) measurements at low-temperature (195-300 K for SrM, 125-300 K for SrM3, SrM7, and 115-300 K for SrM5) for Mn substituted compounds are shown in Fig. S10. ρ decreases gradually with an increase in temperature, thus validates semiconductor-like behavior, i.e. negative temperature coefficient of resistance (NTCR). The ρ also decreases with the Mn substitution. For T < ~175 K, the variable range hopping (VRH; ($\rho = \rho_V exp(T_V/T)^{0.5}$, ρ_V, T_V are coefficient and characteristic temperatures of VRH mechanism respectively) equation fits well and above ~200 K, the Arrhenius equation fits properly. The Arrhenius equation ($\rho = \rho_0 exp(T_0/T)$, ρ_0= constant and $T_0 = E_a/k_B$, E_a= activation energy for conduction, k_B = Boltzmann constant), indicates towards nearest-neighbor hopping phenomena (NNH; $\rho \propto exp(1/T)$). The natural log of DC electrical resistivity versus temperature (1000/T) is shown in Fig. S10 inset (satisfying the NNH mechanism). The activation energy obtained from the fitting is provided in Table S7. The activation energy decreases with the Mn substitution (with a slight increase for SrM7) makes the mobility of charge carriers faster and conductivity increases.
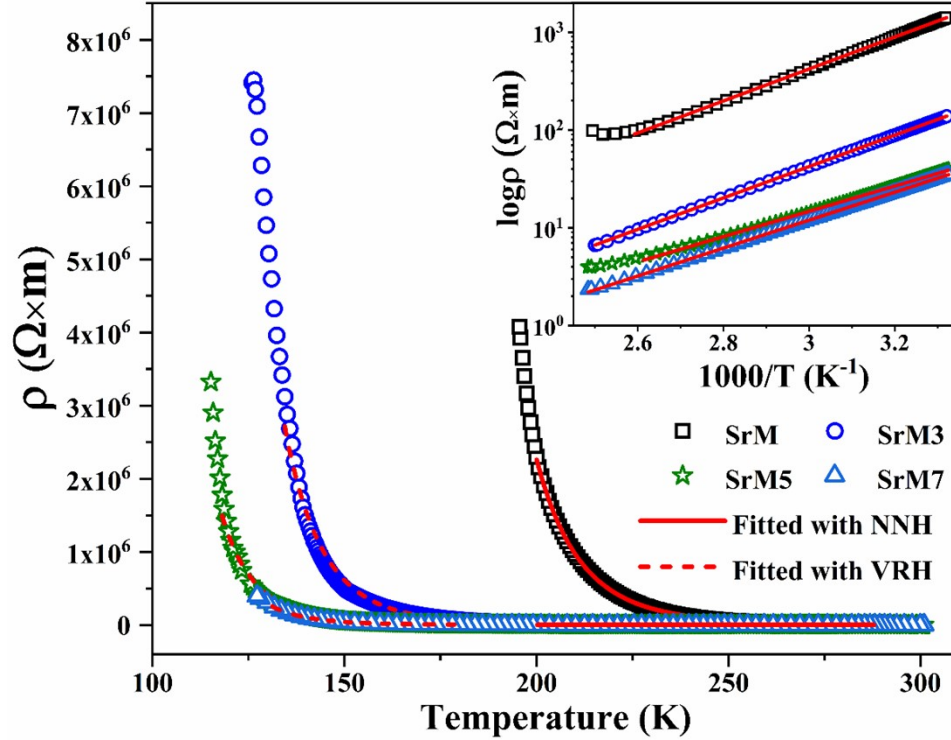
Fig. S10 Plot of DC- resistivity (ρ) vs temperature for all the compounds are shown. In the inset, the DC- resistivity (ρ) measurement in 300 K - 400 K is shown for the same. The solid line and dashed line are for the fitting lines satisfying NNH and VRH respectively.

Table S7. Fitting parameters of resistivity measurement for the LTR.

	VRH (T< ~175K)		NNH (~200K ≤ T ≤~300K)		
Parameters $\longrightarrow$ Samples $\downarrow$	$\rho_V \times 10^{-6}$	$T_V \times 10^5$	$\rho_0 \times 10^{-3}$	$T_0 \times 10^3$	E_a (eV)
SrM			46.08(2)	3.45(2)	0.32(2)
SrM3	1.90(1)	1.05(3)	6.48(2)	2.99(4)	0.30(1)
SrM5	1.55(4)	0.90(1)	3.94(1)	2.65(3)	0.25(3)
SrM7	0.31(3)	0.98(3)	1.75(3)	2.71(3)	0.28(4)

REFERENCES

1S R. Tang, H. Zhou, W. You, and H. Yang, Appl. Phys. Lett., 2016, **109**, 082903.

2S J. Jianga, L.H. Ai J. S. Marcos, J. Alloys Compd., 2010, **502**, 488.

3S S. Kumar, S. Supriya, R. Pandey, L.K. Pradhan, R.K. Singh, and M. Kar, J. Magn. Magn. Mater, 2018, **458**, 30.

4S K. Kimura, M. Ohgaki, K. Tanaka, H. Morikawa and F. Marumo, J. Solid State Chem., 1990, **87**, 186.

5S J. M. D. Coey, Magnetism and Magnetic Materials, 1st ed., Cambridge University Press, 2010.